Volume 8
Number 42
14 November 2020
Pages 21885–22438

Journal of Materials Chemistry A

Materials for energy and sustainability

rsc.li/materials-a

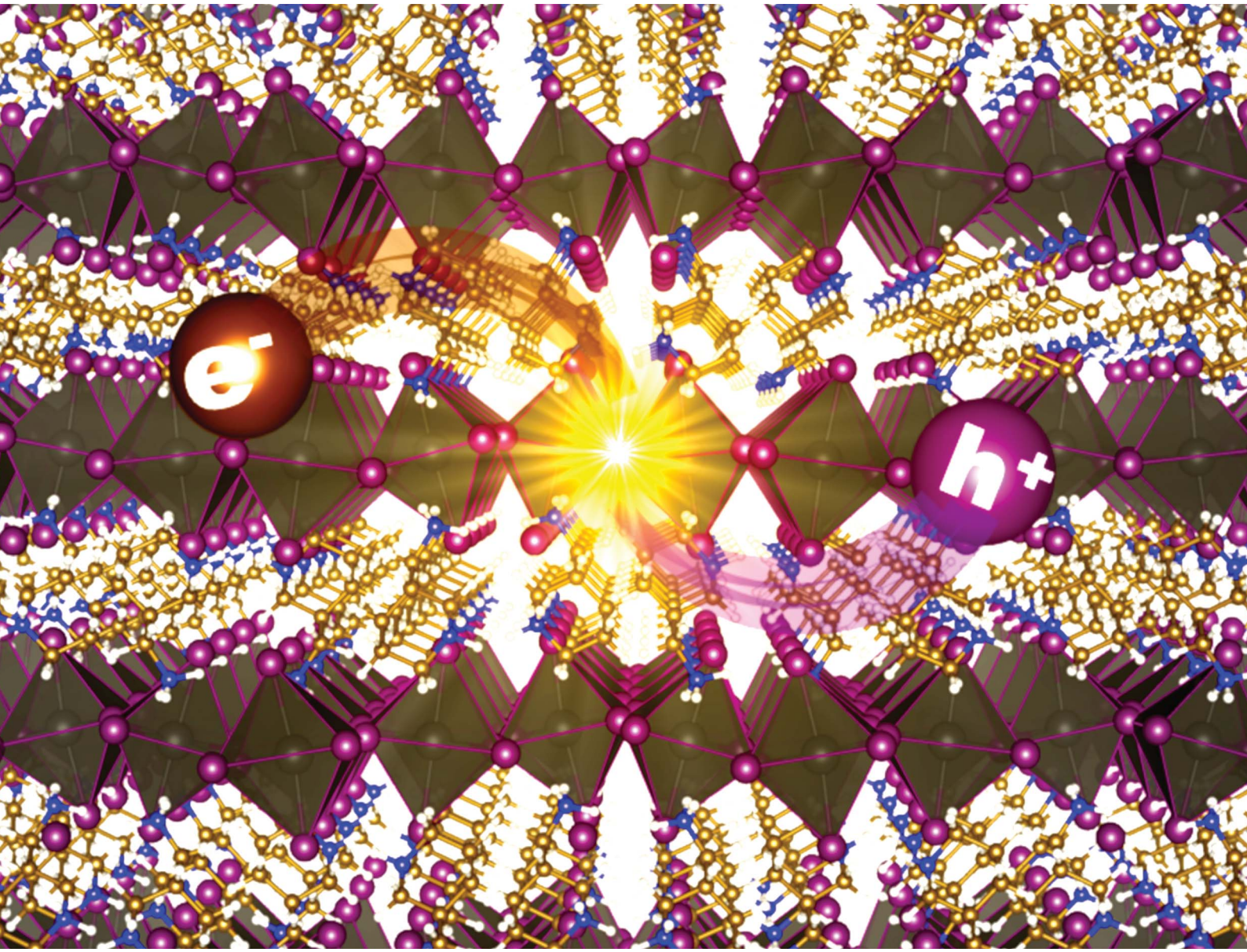

ISSN 2050-7488

ROYAL SOCIETY OF CHEMISTRY

PAPER

Dibyajyoti Ghosh, Amanda J. Neukirch *et al.*
Charge carrier dynamics in two-dimensional hybrid perovskites: Dion–Jacobson *vs.* Ruddlesden–Popper phases

Journal of Materials Chemistry A

ROYAL SOCIETY OF CHEMISTRY

PAPER

View Article Online
View Journal | View Issue

Cite this: J. Mater. Chem. A, 2020, 8, 22009

Charge carrier dynamics in two-dimensional hybrid perovskites: Dion–Jacobson *vs.* Ruddlesden–Popper phases†

Dibyajyoti Ghosh, *[ab] Debdipto Acharya,[cd] Laurent Pedesseau, [d] Claudine Katan, [e] Jacky Even, [d] Sergei Tretiak[abf] and Amanda J. Neukirch*[a]

Two-dimensional (2D) halide perovskites are promising materials for environmentally stable next-generation optoelectronic device applications. Besides the widely investigated Ruddlesden–Popper (RP) phases, Dion–Jacobson (DJ) phases are attracting considerable attention due to their rapid emergence as efficient solar cell materials. However, there is very little atomistic understanding of the charge carrier dynamics under ambient conditions for these DJ-phases, limiting the possibilities to tune their optoelectronic performances through compositional engineering routes. Here, by combining nonadiabatic molecular dynamics with time-domain density functional theory methods at room temperature, we compare the dominant non-radiative carrier recombination and dephasing processes in RP and DJ monolayered lead halide perovskites. Our systematic study demonstrates that performance-limiting nonradiative carrier recombination processes greatly depends on the electron–phonon interactions induced by structural fluctuations and instantaneous charge localization in these materials. The stiffer interlayer packing due to the presence of single spacer dications, which separates the lead iodide slabs, reduces the thermal fluctuations in the DJ-phase to a greater extent than that in the RP-phase 2D-perovskites. Specific electronic coupling between the closely spaced lead iodide layers enhances the delocalization of band-edge charge densities in DJ-phase systems. Compared to the RP-phase, reduced inelastic electron–phonon scattering in DJ-phase perovskites significantly limits intrinsic non-radiative recombination processes. The consequent enhancement in the photogenerated charge carrier lifetime makes DJ-phase perovskites potentially suitable for various optoelectronic devices. The computational insights gained from this study allow us to outline a set of robust design principles for DJ-phase perovskites to strategically tune their optoelectronic properties.

Received 23rd July 2020
Accepted 27th August 2020

DOI: 10.1039/d0ta07205b

rsc.li/materials-a

Introduction

Low-dimensional lead halide perovskites are promising candidates for a variety of stable optoelectronic devices such as solar cells,[1–3] light-emitting diodes,[4,5] photocatalysts,[6–8] and photo- and radiation detectors.[9] Particularly, two-dimensional (2D) iodide perovskites attract significant research interest due to their long-term stability under ambient conditions, significant moisture resistance, rich chemical and structural diversity, and consequently widely tunable photovoltaic properties.[4,5,10–13] In these materials, halide perovskite layers remain separated by long organic spacer cations (Fig. 1a–c). Among several 2D-halide perovskite structures, extensive studies of Ruddlesden–Popper (RP) phases have demonstrated their possible applications in solar cells, color-pure photo-emitting diodes, X-rays, and photo-detectors.[14–19] More recently, Dion–Jacobson (DJ) phases have emerged as another family of layered halide perovskites that exhibit promising efficiency in solar cell devices.[20–27] The difference between these 2D-perovskites originates from the fact that a RP-phase contains two monocationic spacers whereas a DJ-phase contains only one dication spacer molecule per formula unit. The common chemical formulas of RP and DJ-

[a]Theoretical Division, Los Alamos National Laboratory, Los Alamos, NM, 87545, USA. E-mail: dibyajyoti@lanl.gov; ajneukirch@lanl.gov

[b]Center for Nonlinear Studies, Los Alamos National Laboratory, Los Alamos, NM, 87545, USA

[c]Theoretical Sciences Unit, Jawaharlal Nehru Centre for Advanced Scientific Research, Bangalore, 560064, India

[d]Univ Rennes, INSA Rennes, CNRS, Institut FOTON – UMR 6082, F-35000 Rennes, France

[e]Univ Rennes, ENSCR, INSA Rennes, CNRS, ISCR – UMR 6226, F-35000 Rennes, France

[f]Center for Integrated Nanotechnologies, Los Alamos National Laboratory, Los Alamos, NM, 87545, USA

† Electronic supplementary information (ESI) available: Details of $(BA)_2PbBr_4$ and $(PEA)_2PbBr_4$ structures, charge carrier dynamics in these perovskites, and fitting of carrier recombination functions. See DOI: 10.1039/d0ta07205b

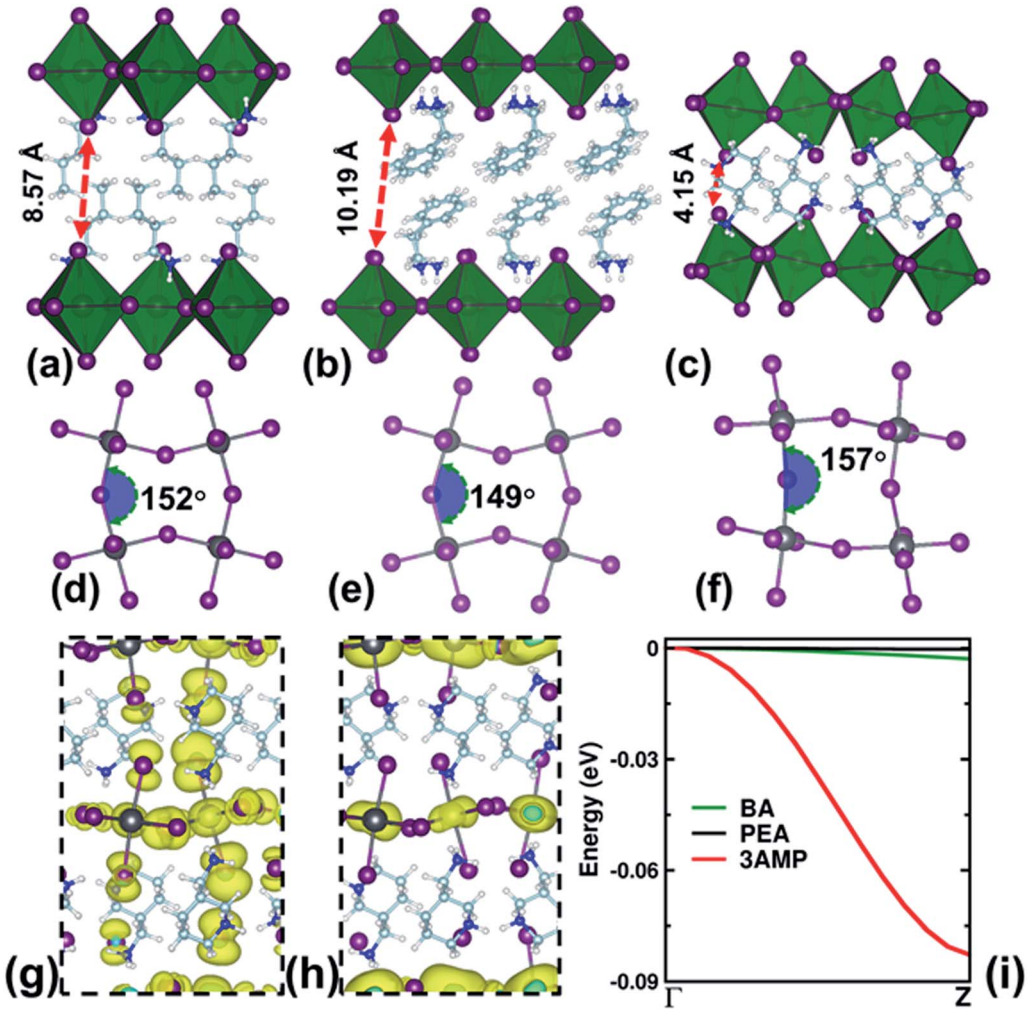

Fig. 1 Optimized structures and electronic properties of 2D-perovskites. DFT-based optimized structures of (a) $(BA)_2PbI_4$, (b) $(PEA)_2PbI_4$ and (c) (3 AMP)PbI_4. Colors: hydrogen (white), carbon (black), nitrogen (blue), iodine (pink), and lead (grey). The dashed red lines and numbers show the average distances between the interlayer axial I atoms. (d–f) The equatorial Pb–I plane and Pb–I–Pb angles of the optimized structures as shown in (a–c). The deviation of Pb–I–Pb angles from linearity (*i.e.* 180°) characterizes the extent of PbI_6 octahedral distortion. The electronic charge densities of (g) VBM and (h) CBM for (3AMP)PbI_4. The band edge charge densities are delocalized over the inorganic layer. The closely spaced axial I atoms form interlayer coupling in the VBM state. The electronic structures are calculated using the PBE-GGA + SOC level of theory (see the Methods). (i) Comparison of valence band dispersion curves along the stacking axis for these 2D-perovskites.

phases are $A'_2A_{n-1}B_nX_{3n+1}$ and $A''A_{n-1}B_nX_{3n+1}$, respectively where A′ is a monocation and A″ is a dication-based spacer molecule. In these chemical formulas A is a smaller organic or inorganic cation (such as methylammonium or Cs), B is a divalent metal, and X is a halogen. B_nX_{3n+1} constructs the inorganic layer, containing corner-shared BX_6 octahedra, and spacer cations (*i.e.* A′ and A″) non-covalently hold these inorganic slabs. The thickness of the inorganic layer depends on the parameter n that represents the number of BX_6 layers in each B_nX_{3n+1}. In most of the RP and DJ-phases reported to date, the B_nX_{3n+1} layer plays a central role in the basic optoelectronic properties such as the band gap, carrier mobility, and optical absorption.[20,22,28–30] The organic spacer cations do not directly affect electronically the band edge characteristics, but influence the structural distortions in the B_nX_{3n+1} layer and interlayer charge screening through image charge effects.[31,32] These effects, when they are considered as static effects, already impact important properties such as the optical band gap, exciton binding energy, and carrier mobility in 2D halide perovskites. Recent in-depth studies further revealed more subtle roles of these spacer cations in determining the photophysical properties of mechanically 'soft' 2D-perovskites at room temperature.[33–39] The geometry and chemical bonding in the inorganic sublattices and their non-covalent interactions with organic spacers lead to substantial structural dynamics in these halide perovskites under ambient conditions. Strong and complex dynamic coupling between the inorganic layer and the spacer cations significantly enhances the electron–phonon interactions, increasing the non-radiative charge recombination rates.[38,40] In this recombination process, the electronic energy of photo-generated carriers gets rapidly transferred to the vibrational motions of the lattice, significantly deteriorating

the performance of an optoelectronic device. Several approaches, such as including π-stacked spacer cations, increasing the thickness of the inorganic layers, and monovalent cation mixing have been investigated to try mitigating the non-radiative carrier losses in RP and also 3D halide perovskites.[35–39] At the atomistic level, all these approaches result in an increase of the organic and inorganic sublattice stiffness. This weakens the electron–phonon coupling at room temperature and consequently prolongs the photo-generated carrier lifetime. In the DJ-phase, the presence of a single dicationic spacer molecule provides unique opportunities to enhance the lattice stiffness by (1) introducing non-covalent interlayer halogen interactions between inorganic slabs and (2) by avoiding the floppiness of the organic barrier induced by the intermolecular van der Waals interactions in the spacer cation layer. These specific structural features should reduce the low-frequency structural fluctuations of the lattice, and therefore weaken the thermally induced electron–phonon coupling, and result in a longer carrier lifetime. Furthermore, the non-covalent interlayer halogen interactions also promote increased electronic coupling between the layers and enhance the carrier delocalization.[20,24,26] A recent time-resolved photoluminescence spectroscopy-based study has indeed reported that the average carrier lifetime for the DJ lead iodide perovskite is twice that of the RP-phase.[27] The longer carrier lifetime underpins the observed enhancement of the DJ perovskite-based planar heterojunction solar cell efficiency to >17%. These promising preliminary reports demand a more in-depth atomistic investigation of the charge carrier dynamics in the DJ-phase than has been done so far.[25] The fundamental structure–optoelectronic property relationships suggest further guidelines for efficient low-dimensional photoactive material design and discovery. Particularly, a wide variety of possible short-length diamine molecules may serve as organic spacers thus providing extensive compositional space for fine-tuning the photophysical properties of these emerging layered perovskites.

Following our previous investigations of the dynamic structure–property relationships in low-dimensional and 3D-halide perovskites,[15,16,41–43] the current work combines *ab initio* real-time time-dependent density functional theory (DFT) and non-adiabatic molecular dynamics (NAMD) modeling to systematically study the intrinsic and room temperature non-radiative charge carrier recombination in RP and DJ lead iodide perovskite phases. To underline the importance of spacer cations, we only consider single layer ($n = 1$) 2D-perovskites that do not contain 3D bulk-like slabs. It also allows addressing complex non-adiabatic carrier dynamics at a reasonable computational cost. Due to their well-characterized phase-pure synthesis, single layer 2D-perovskites have been investigated extensively to evaluate the fundamental structure–property relationships.[35,44–50] We consider RP-phase A'_2PbI_4 2D-perovskites with two commonly explored cations, long alkyl chain *n*-butylammonium (BA) and benzene ring containing phenylethylammonium (PEA).[15,29,51,52] A comparison between these systems reveals the effects of stacked aromatic ring spacer cations on the structural dynamics and charge carrier recombination processes. Among the experimentally synthesized DJ-phase perovskites, we chose the structurally well-characterized (aminomethyl)piperidinium (3AMP) based (3AMP)PbI_4 as the representative DJ system for our study.[20] Restricted structural dynamics and charge delocalization through PbI_4 interlayer stacking in (3AMP)PbI_4 significantly reduce the non-radiative recombination of photo-generated free carriers, prolonging the carrier lifetime. Overall, we find better photophysical characteristics for DJ-phase perovskites compared to RP-phase ones. By exploring at the atomic scale the relationships between the structural and charge carrier dynamics, our study reveals the subtle effects of electron–phonon interactions on the recombination processes in photoactive 2D iodine perovskites. We emphasize the importance of spacer cation engineering strategies to improve the performances of layered perovskite-based optoelectronic devices.

Results and discussion

Static structural properties

The optimized ground-state geometries of $(BA)_2PbI_4$, $(PEA)_2PbI_4$, and (3AMP)PbI_4 shown in Fig. 1 demonstrate key differences that arise from the inorganic layer–spacer cation non-covalent interactions. In all systems, the single-layer PbI_6 octahedra exhibit corner-shared connectivity and have similar Pb–I bond lengths. However, due to the single and short spacer dication in (3AMP)PbI_4, the PbI_6 octahedral slabs form interlayer van der Waals interactions that are completely absent in the investigated RP-phase perovskites (Fig. 1a–c). In (3AMP)PbI_4 the interlayer axial I⋯I distances range from 4.13 Å to 4.21 Å, being lower that the van der Waals diameter of iodine atoms (∼4.44 Å).[20,53] These non-covalent interactions in (3AMP)PbI_4 introduce interlayer coupling between perovskite slabs.[20] Moreover, the equatorial Pb–I–Pb angles differ where (3AMP)PbI_4 has less overall distortion and more linear angles compared to $(BA)_2PbI_4$ and $(PEA)_2PbI_4$ (Fig. 1d–f). However, despite the denser packing of the organic barrier in the DJ-phase, all the structures have seemingly similar H_3N–I (equatorial) distances from a static viewpoint. This important aspect will be clarified from a dynamical viewpoint (*vide infra*).

Static electronic properties

We investigate the ground-state electronic structures of 2D-perovskites with the optimized structures obtained from DFT-based simulations (see the Methods). When including spin–orbit coupling (SOC) corrections, the calculated electronic band gaps are 1.18 eV, 1.34 eV and 1.37 eV for (3AMP)PbI_4, $(BA)_2PbI_4$ and $(PEA)_2PbI_4$, respectively. Except the systematic and expected underestimation of electronic band gaps compared to the well documented experimental data, the PBE + SOC level of theory is a reliable approach to capture the electronic band gap trend of halide perovskites and their overall electronic structures.[31,42,54–56] The electronic band gap underestimation originates due to the absence of electronic many-body interactions which are prohibitively expensive to include in the simulations for such large structures.[54,57,58] The band-edge charge densities and the projected density of states show that both the valence

band maximum (VBM) and the conduction band minimum (CBM) are delocalized over the Pb–I framework, without any identifiable contributions from the organic spacer cations (Fig. 1g, h and S5†).[31,59] The VBM has contributions from the σ-antibonding overlap between the 5p orbitals of I and 6s orbitals of Pb (Fig. 1g, S5 and S6†), whereas the dominant contribution to the CBM comes from the Pb 6p orbitals along with small contributions from I 5p orbitals forming σ-antibonding overlap (Fig. 1h, S5 and S6†). The details of orbital overlaps and bonding types at the band edges further illustrate the structure–optoelectronic property relationship in these 2D-perovskites. A more linear equatorial Pb–I–Pb angle (that is close to 180°) enhances the s–p orbital overlap between Pb and I. Due to the anti-bonding nature of the VBM, such an increased orbital overlap results in an up-shift in the valence band edge energy level. As discussed in previous studies, it mainly causes a reduction in the band gap for more linear PbI_6 octahedral connectivity.[42,43,59–61] Thus, in general, the smaller the Pb–I–Pb angle distortion, the smaller the electronic band gap in halide perovskites. This structure–property relationship explains most computed electronic band gap variations of the 2D-perovskites; as the average Pb–I–Pb equatorial angles reduce (3AMP)PbI_4 > $(BA)_2PbI_4$ > $(PEA)_2PbI_4$, the electronic band gap follows the opposite trend.[60,61]

Additionally, the axial iodide atoms of consecutive perovskite layers in (3AMP)PbI_4 undergo non-covalent interactions as the I⋯I distances (4.13–4.21 Å) remain lower than their van der Waals diameter (≈4.4 Å). Considering the charge density of the VBM as shown in Fig. 1g (3D) and in Fig. S7† (2D), the repulsive electrostatic interaction between the axial I-5p orbitals further destabilizes the valence band edge and shifts its energy level upward.[20] The CBM state, however, remains mostly unaffected from these non-covalent interactions due to its in-plane charge density distribution (Fig. 1h). Therefore, the interlayer halogen interaction contributes to the red-shift of the band gap value of (3AMP)PbI_4. Due to the large lead iodide interlayer distances in RP-phase 2D-perovskites, the axial I⋯I pairs remain spatially apart (>8.5 Å), making the electronic coupling along the stacking axis and its effects on the electronic band gap negligible.

Fig. 1i shows the band structures along the stacking direction (*c*-axis), $\Gamma \rightarrow Z$, which emphasizes the dispersive nature of the valence band only for (3AMP)PbI_4. This further confirms the unique interlayer electronic coupling in the DJ-phase perovskite due to the shorter interlayer PbI distances. The VBM remains largely flat for $(BA)_2PbI_4$ and $(PEA)_2PbI_4$, depicting the lack of perovskite interlayer halogen interactions in these systems. VBM dispersion may be more favorable for interlayer hole transport in the DJ-phase perovskites compared to the RP-phase materials. However, the conduction band edges that have a dominant contribution of the non-bonding Pb-5p state remain mostly alike in terms of band dispersion for all of the 2D-perovskites (see Fig. S8†).

Dynamic structural properties

At finite temperature, structural dynamics significantly influences the instantaneous geometry and charge carrier dynamics in halide perovskites.[35,44,62–64] Thus, we perform *ab initio* molecular dynamics (AIMD) simulations at 300 K to explore the dynamical behavior of these 2D-perovskites (see the Methods).

We compute the root mean square fluctuations (RMSF) for individual inorganic sites and organic cations of 2D-perovskites to apprehend the overall extent of thermally induced fluctuations in these materials. As shown in Fig. 2, each individual component of $(BA)_2PbI_4$ has the highest RMSF value, revealing that this BA-based perovskite has the largest structural fluctuations. Due to the π–π interactions enhancing the stiffness along the cations stacks, the thermal distortions of the perovskite and organic layers are considerably suppressed in $(PEA)_2PbI_4$ compared to the long alkyl cation based $(BA)_2PbI_4$.[35] The dicationic spacers in (3AMP)PbI_4 do not have the van der Waals gap in the spacer layer and the short dications allow for the formation of non-covalent halogen interactions between two neighboring perovskite slabs. This further restricts the thermal motions of Pb and 3AMP cations. As the single perovskite layers in all of these 2D-perovskites are chemically identical, it is evident that the spacer cations are the origin of variations in the overall structural rigidity and dynamics under ambient conditions. Therefore, the choice of spacer cations is an effective tool to fine-tune the dynamical behavior of low-dimensional halide perovskites.

The dynamical structural study shows a sizable difference in RMSF between DJ and RP-phases, which already indicates the importance of the mechanical coupling between the inorganic lattice and the cations in the barrier. Closer inspection reveals that differences in the equatorial Pb–I–Pb bond angle fluctuations in these 2D-perovskites can be attributed to the steric interaction with spacer cations. The intrusion depth of the NH_3 group into the open grooves of perovskite layers produces steric effects exerted by the spacer cations on the inorganic layer, which is distinct for DJ and RP-phases. From the viewpoint of the inorganic layer, the most striking difference between the three systems is related to the equatorial Pb–I–Pb bond angle thermal distributions (Fig. 3a). (3AMP)PbI_4 exhibits a skewed distribution with a Pb–I–Pb mode angle (that is the most common angle) at 162.4° (Fig. 3a). The RP-phase PEA and BA cation-based perovskites have a Gaussian-type distribution around a more distorted average structure with mode angles at 148.4° and 151.8°, respectively. It is well known that such distortions deeply affect the electronic structure of 2D-

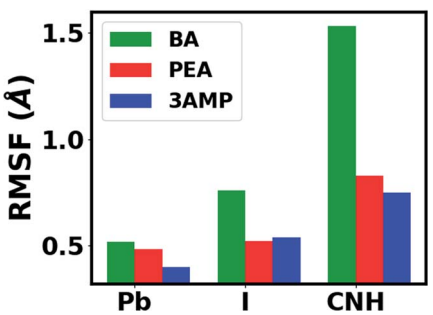

Fig. 2 Influences (RMSF) of the spacer cations on the lattice thermal fluctuations for 2D-perovskites. The root mean square fluctuations for Pb, I, and organic spacers at 300 K for DJ- and RP-phase perovskites.

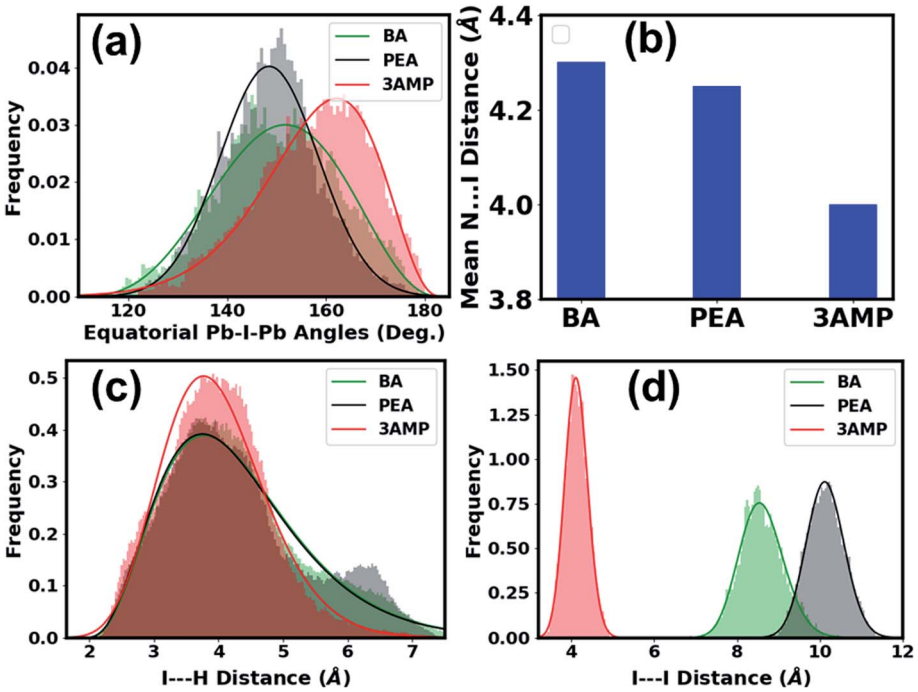

Fig. 3 Structural dynamics at 300 K in 2D-perovskites. (a) The histograms of equatorial Pb–I–Pb bond angles computed over AIMD simulation trajectories of all three 2D-perovskites. (b) The mean distances between the in-plane I of the inorganic equatorial plane and N atoms of the NH_3 group of spacer cations. The histograms of (c) the distances between the in-plane I and H atoms of NH_3 of spacer cations and (d) the axial I⋯I distances between two stacked inorganic layers. We fit the distributions with the beta distribution function as plotted by the solid line.

perovskites.[59,60] From the viewpoint of the organic spacers, differences between DJ and RP-phases are also revealed by the dynamical study. The distances between the equatorial iodide atoms and the nitrogen atom of the NH_3 group in the spacer cations reveal the fluctuations of the intrusion depth (Fig. S1a and b†). As shown in Fig. 3b, the time averaged distances point to shorter N⋯I lengths in (3AMP)PbI_4 compared to the mono-cationic RP-phase perovskites. Short N⋯I lengths are consistent with a deeper intrusion depth and reduced spatial separation between the spacer and inorganic frame, imposing steric constraints on the Pb–I equatorial plane of PbI_6 octahedra. In response to this steric crowding in (3AMP)PbI_4, the equatorial inorganic plane expands, making the average Pb–I–Pb angles relatively linear and increasing instantaneous angle values compared to the RP-phase 2D-perovskites (Fig. 3a). The increased average equatorial Pb–Pb distance in 3AMP-based perovskites also supports the spacer cation induced in-plane expansion of their perovskite layers (see Fig. S2† for details). The Pb–I bond length dynamics exhibit similar distributions for all three 2D-perovskites as detailed in the ESI, Section S1.†

To further analyze the dynamical interactions between the inorganic and organic sublattices, we calculate the distances between the H atoms of the NH_3 group in the spacer and the iodide of the Pb–I equatorial plane (Fig. S4†). As demonstrated in previous studies, these non-covalent interactions form hydrogen bonds between the inorganic and organic sublattices, influencing their coupled thermal motions at finite temperatures.[41,42,65,66] In Fig. 3c, the N–H⋯I distance in the DJ-phase is more narrowly distributed compared to that in the RP-phase perovskites. The narrow distribution of this non-covalent bond suggests consistent dynamical coupling between perovskite layer and spacer cations in (3AMP)PbI_4.[42,43] Furthermore, the ensemble average of N–H⋯I is shorter for the DJ-phase (3.9 Å) compared to RP-phase perovskites (≈4.3 Å). At a qualitative level, considering the dominant electrostatic nature of this non-covalent interaction, the shorter average N–H⋯I distance indicates stronger hydrogen bonding interactions in (3AMP)PbI_4.[67] Such hydrogen-bond formation, in turn, partially restricts the thermal motions of the equatorial iodine acceptor sites in the DJ-phase as discussed in the ESI (Section S2).† A quantitative description of the dynamic hydrogen bonding interactions can be explored by path-integral MD that is beyond the scope of the present work.[68–70]

Other structural features unique to DJ-phase perovskites are the short interlayer distances between inorganic layers. As shown in Fig. 3d, the axial iodine atoms maintain short interlayer I⋯I distances (≈3.2–5.0 Å) throughout the AIMD trajectory. These reduced instantaneous I⋯I distances indicate a strong dynamical interlayer coupling between the inorganic layers in (3AMP)PbI_4. Due to the significantly larger interlayer spacing between inorganic layers, structural fluctuations do not induce fluctuations of the interlayer electronic coupling in RP-phase 2D-perovskites (Fig. 3d). As discussed later, the presence of the interlayer electronic coupling influences the optoelectronics of DJ-phase 2D-perovskites to a noticeable extent. It is worth mentioning that as we perform AIMD with constant experimental cell parameters, volume relaxation induced structural fluctuations are not included in

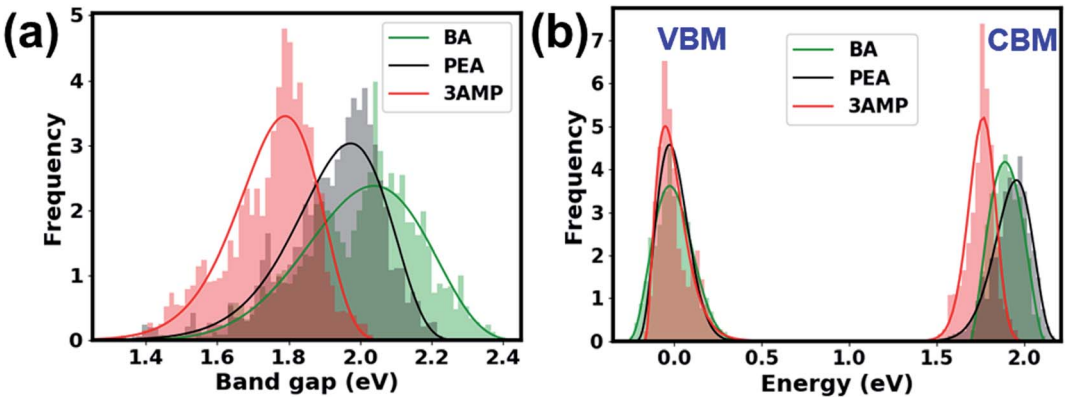

Fig. 4 Dynamic electronic structures in 2D-perovskites. (a) The histogram distribution of band gaps along the AIMD trajectories for 2D-perovskites. The DJ-phase perovskite exhibits narrowly distributed and red-shifted band gaps at room-temperature. The distribution characters remain unchanged with the inclusion of SOC corrections as shown in Fig. S9.† (b) The thermal broadening in the VBM and CBM states of $(BA)_2PbI_4$, $(PEA)_2PbI_4$, and (3AMP)PbI_4. Both the VBM and CBM are narrowly distributed for DJ-phase perovskites, indicating a less thermal broadening of their band edge states. All band edge energies of a particular system are scaled to their average of VBM state energy. Solid lines are fitted with the beta function to the distributions of data.

the simulations. However, we expect similar overall structural dynamics even after considering such fluctuations in these 2D-perovskites.[71]

Adiabatic fluctuations of the electronic properties

To explore the direct influence of finite-temperature structural dynamics on the optoelectronic properties of 2D-perovskites, we next plot the electronic band gap distribution calculated along the AIMD trajectories (Fig. 4a). As shown in the histograms, (3AMP)PbI_4 exhibits the most narrowly distributed and distinctly red-shifted band gaps over time among all the 2D-perovskites considered here. The average and standard deviations of the electronic band gap distributions for all 2D-perovskites are listed in Table 1. These distributions demonstrate that the equatorial Pb–I–Pb bond angle is the dominant descriptor affecting the instantaneous electronic band gap of both RP and DJ-phase 2D-perovskites. As Pb–I–Pb angles in (3AMP)PbI_4 skew towards higher values $\approx 162^\circ$, the PbI_6 octahedra are less distorted in this perovskite (Fig. 3a), red-shifting its electronic band gap distribution. Furthermore, considering two RP-phase perovskites, the narrower Pb–I–Pb angle distribution of $(PEA)_2PbI_4$ results in less dispersed band gap values than that in $(BA)_2PbI_4$.

To demonstrate the robustness of the observed electronic band gap distributions in terms of applied computational methods, we further incorporate SOC corrections for evaluating the instant electronic band gaps along the simulated trajectories. The SOC effect substantially alters the band edge electronic properties in halide perovskites.[31,54,58,72] To offset the numerical cost due to the inclusion of SOC, we consider hundreds of instant structures, equally spaced in the simulation time for band gap evaluation. As we have discussed, the incorporation of SOC corrections in the absence of many-body electronic effects underestimates the band gaps by ≈ 1 eV.[42,73] Fig. S8† shows that the characteristics of the electronic band gap distributions obtained with SOC corrections closely resemble those calculated with plain PBE-GGA. Thus, the computationally cheap semi-local functionals can reasonably capture the qualitative nature of band gap fluctuations in 2D-perovskites that are dominantly influenced by the structural dynamics under ambient conditions.

To understand the impact of structural fluctuations on the individual band-edge states, we compute the relative position of VBM and CBM energy states over the simulation time. In Fig. 4b, both the VBM and CBM exhibit narrower distributions for (3AMP)PbI_4 compared to $(BA)_2PbI_4$ and $(PEA)_2PbI_4$ (Table S1, ESI†). While the distribution in the VBM energy state mainly originates from the fluctuations in the equatorial Pb–I–Pb angles, the displacement in Pb sites dominantly controls the instant relative position of the CBM state. The skewed and narrower distribution of Pb–I–Pb angles (Fig. 3a) and smaller RMSF of Pb atoms (Fig. 2) in DJ-phase perovskites lead to their sharper band edges compared to RP-phase perovskites. Narrow distributions of both band edges consequently contribute to reduced band gap fluctuations in (3AMP)PbI_4 as we find in Fig. 4a.

Table 1 The calculated electronic band gaps, average and standard deviation (stdv) of PBE band gap values along AIMD trajectories, nonradiative carrier recombination times, and pure-dephasing time for $(BA)_2PbI_4$, $(PEA)_2PbI_4$ and (3AMP)PbI_4

Perovskites	Static PBE + SOC (PBE) band gap (eV)	Average PBE band gap (eV) (stdv)	Recombination (ns)	Pure-dephasing (fs)
$(BA)_2PbI_4$	1.34 (2.09)	2.00 (0.16)	4.9	5.0
$(PEA)_2PbI_4$	1.37 (2.12)	1.92 (0.14)	14.5	4.8
(3AMP)PbI_4	1.18 (1.92)	1.75 (0.12)	79.7	5.7

Importance of non-adiabaticity for non-radiative recombination

The finite-temperature induced structural distortions play a decisive role in photo-generated charge carrier dynamics in low-dimensional halide perovskites.[38,40] We employ non-adiabatic molecular dynamics (NAMD) with real-time time-domain DFT to investigate the comparative impact of structural dynamics on the non-radiative carrier recombination rate in RP- and DJ-phases of lead iodide perovskites. As shown in Fig. 5a, the evolution of carrier populations with time depicts a much faster rate of photo-generated charge recombination in $(BA)_2PbI_4$ compared to both $(3AMP)PbI_4$ and $(PEA)_2PbI_4$. Using the short-time linear approximation of the exponentially increasing function (discussed in the Methods[38,74]) we find that the non-radiative carrier life-times are 4.9 ns, 14.5 ns, and 79.7 ns for $(BA)_2PbI_4$, $(PEA)_2PbI_4$, and $(3AMP)PbI_4$, respectively (Table 1). The overall trend and longer carrier lifetime of the DJ-phase lead iodide perovskites are consistent with those in recent experimental reports.[24,27,75] Moreover, the estimated carrier lifetimes for all the 2D-perovskites are on the nanosecond time scale, matching reasonably well with the time-scale of respective experimental values.[24,27,47,76] Thus, our study unambiguously demonstrates that the spacer molecules have an important influence on the charge carrier recombination dynamics in 2D-halide perovskites. The additional influence of interlayer electronic coupling related to iodine atoms will be demonstrated in the next part.

The dynamic coupling between the electronic and lattice degrees of freedom affects the non-radiative charge relaxation and recombination processes that directly impact the performance of perovskite-based optoelectronic devices.[38,74,77,78] As key factors such as electron–phonon interactions and energy gaps dominantly influence the non-radiative carrier recombination, we further investigate these aspects in detail.

The electron–phonon interactions at finite temperature involve both elastic and inelastic carrier scattering in hybrid materials.[38,74,79,80] Under ambient conditions, an energy exchange between electronic and vibrational subsystems occurs through the inelastic scattering mechanism. In this process, during non-radiative recombination, the extra energy that is generated from the recombined charges is dissipated to the nuclear degrees of freedom.[81] To quantify the strength of this scattering process, the non-adiabatic coupling (NAC) constants

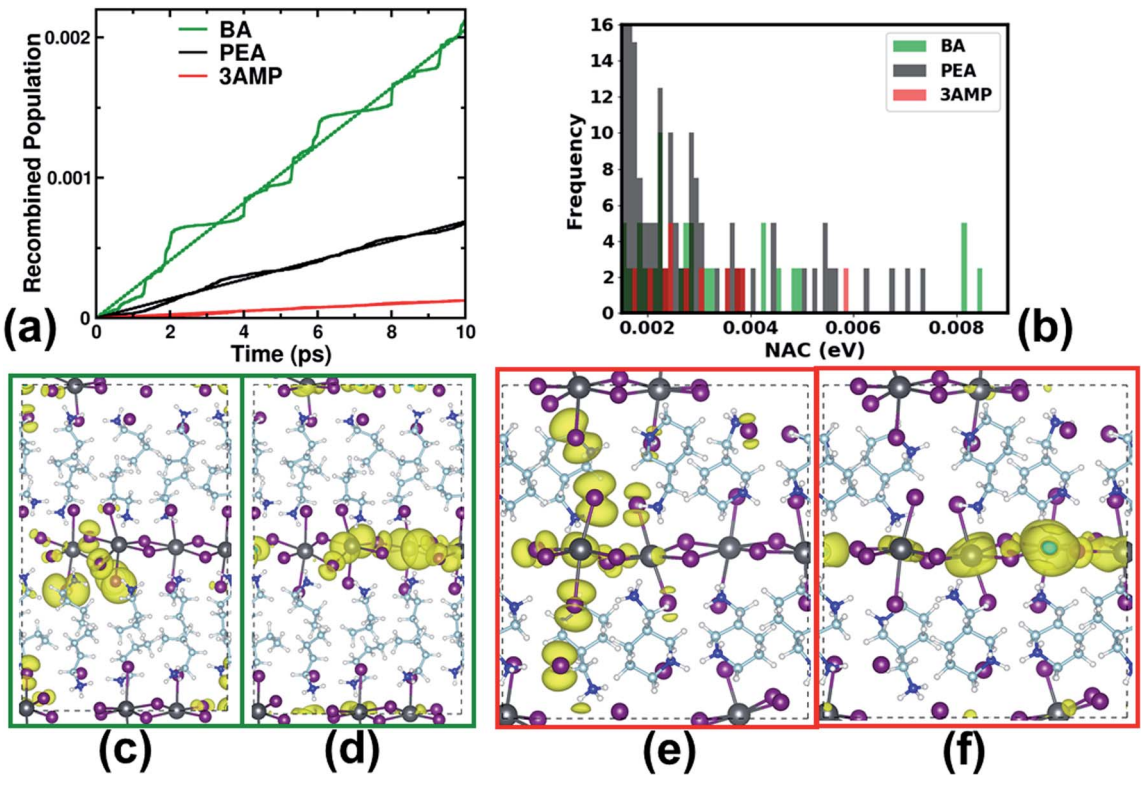

Fig. 5 The nonradiative carrier recombination and nonadiabatic coupling (NAC) in 2D-perovskites. (a) The recombined electron–hole population in $(BA)_2PbI_4$, $(PEA)_2PbI_4$, and $(3AMP)PbI_4$ over time. We fit the time-dependent population increase to $f(t) = 1 - \exp(-t/\tau)$, where τ is the electron–hole recombination time. $(BA)_2PbI_4$ and $(3AMP)PbI_4$ have the fastest and the slowest recombination rates, respectively. (b) The histogram distribution of absolute instantaneous NAC values with magnitude > 0.0015 eV. Plotted NACs are calculated between VBM and CBM states for 2D-perovskites. $(BA)_2PbI_4$ and $(PEA)_2PbI_4$ reveal more occurrences of high instantaneous NAC values over the simulation time. A histogram with a complete range of NAC values has been included in the ESI.† The instant (c) VBM and (d) CBM charge densities for the time steps where the NAC is highest (0.0084 eV) in $(BA)_2PbI_4$. Both the band edges are closely localized, enhancing the overlap between the states. The instant (e) VBM and (f) CBM charge densities of $(3AMP)PbI_4$ at the snapshot of time with the highest NAC (0.0056 eV). The delocalized VBM along the stacking direction is prominent and partially reduces the orbital overlap between band edge states.

have been calculated along the simulated trajectories.[82,83] Physically, a higher value of the NAC signifies a stronger coupling between the electrical and lattice degrees of freedom underpinning inelastic scattering processes and consequently indicating faster charge recombination in a material.[84–86] Note that the intra-band charge relaxation rates in the valence and conduction bands are much higher than those of inter-band relaxation across the electronic band gap.[36,37] Thus, we reasonably approximate that the NAC strength between the VBM and CBM is representative of the limiting inelastic process for the non-radiative recombination. In Fig. 5b, the histograms of the instantaneous NAC values demonstrate frequent occurrences of strong VBM–CBM non-adiabatic coupling in $(BA)_2PbI_4$ and $(PEA)_2PbI_4$ along their MD trajectories. The instantaneous NACs have been calculated for each time step of the AIMD trajectory. The frequent occurrences of high instantaneous NAC values in the RP-phase perovskite indicate frequent opening of non-adiabatic channels by which photo-generated electrons and holes undergo non-radiative recombination. Over the simulation time, it results in a faster increase of the recombined carrier population in the valence band edge of the RP-phase perovskite compared to the DJ-phase one.

To understand the origin of different NAC strengths in the studied 2D-perovskites, we closely examine $(BA)_2PbI_4$ and (3AMP)PbI_4 that exhibit the fastest and slowest recombination rates, respectively. The wavefunction overlap between two participating states at sequential time-steps and phonon velocities gives rise to finite instantaneous NAC values.[83] The stronger the wavefunction overlap and the higher the phonon velocity, the larger the NAC value. Here, we are focused on the electron–hole recombination across the band gap where the dominant participating states are the VBM and CBM. As both the VBM and CBM states are confined to the inorganic frame (Fig. 4a), the thermal fluctuations in the Pb and I sites lead to fluctuations of the overlap between the wavefunctions and are therefore indicative of the magnitude of the NACs. Thus, higher structural fluctuations in Pb–I sites in $(BA)_2PbI_4$ underpin the frequent occurrence of higher NAC values in this 2D-perovskite compared to the DJ-phase systems. We further examine the charge densities of band-edge states for snapshots in time corresponding to the high instantaneous NAC values. As shown in Fig. 5c and d for $(BA)_2PbI_4$, both the VBM and CBM instantaneous charge densities are localized over closely spaced regions of the Pb–I framework. They produce finite wavefunction overlap, resulting in strong non-adiabatic coupling between the band edge states. However, in the case of (3AMP)PbI_4 the band-edge charge densities are delocalized, indicating a weaker overlap between the VBM and CBM states (Fig. 5e and f). The VBM state, in particular, shows extended one-dimensional charge delocalization through the axial I atoms that form interlayer stacking in the DJ-phase perovskite, Fig. 5e. Undoubtedly, the short distances between these axial I atoms open up unique channels for extended charge delocalization in the VBM. Moreover, as the AIMD simulation depicts in Fig. 3d, the close I···I stacking remains intact throughout the trajectory at 300 K, demonstrating continued extended charge delocalization for the valence edge of DJ-phase perovskites. Due to possible SOC effects on the charge distributions in lead halide perovskites, we also calculate the instantaneous band edge electronic properties with the PBE + SOC level of theory. As we find in Fig. S10,† the overall nature of instant VBM and CBM charge distributions in RP- and DJ-phase perovskites remains unchanged in the presence of SOC corrections, demonstrating the robustness of our main conclusions irrespective of the computational methods employed. Thus, both the delocalized band-edge charge densities and reduced structural fluctuations in (3AMP)PbI_4 give rise to smaller NAC values compared to that of $(BA)_2PbI_4$. The partial suppression of NAC-induced electron–hole non-radiative recombination helps to enhance the carrier lifetime for the DJ-phase 2D-perovskite as shown in Fig. 5a. Due to π stacking, the thermal fluctuations and consequently instantaneous NACs are relatively weaker in $(PEA)_2PbI_4$ compared to alkyl spacer-based $(BA)_2PbI_4$. This explains the slower electron–hole recombination rate of PEA-based perovskite.

The molecular dynamics study gave us the first indication of the atomistic origin of the mechanical coupling between the perovskite layer and the cation. To further understand the electron–phonon interactions that originate from complex structural dynamics, we calculate the influence spectra for RP- and DJ-phase 2D-perovskites. Such spectra are obtained by computing the Fourier transform (FT) of the unnormalized autocorrelation function (ACF) of the electronic band gaps over the simulation time.[83] The influence spectra identify the particular phonon modes that are coupled to the electronic subsystem and actively involved in the electron–hole non-radiative recombination processes. For the studied 2D-perovskites, all major peaks in the influence spectra emerge below 400 cm^{-1} (Fig. 6). Therefore, the active phonon modes that encompass the nonradiative carrier relaxation are low-frequency vibrational modes. Several 2D- and 3D-halide perovskites exhibit similar characteristics of influence spectra to those already reported by other studies.[77,79,80,87] Despite the presence of C–H and N–H bonds in spacer cations with high-frequency vibrational modes (>3000 cm^{-1}), only low-frequency

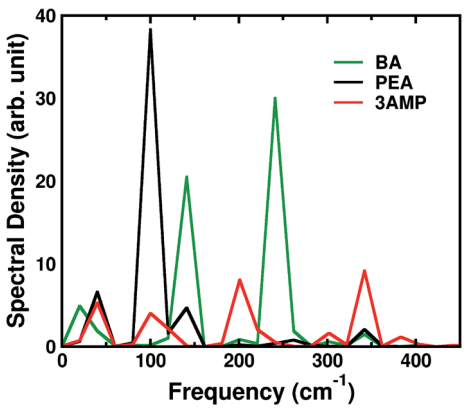

Fig. 6 The electron–phonon interactions in 2D lead iodide perovskites. The Fourier transform of autocorrelation for the band gap fluctuations in $(BA)_2PbI_4$, $(PEA)_2PbI_4$, and (3AMP)PbI_4. The *y*-axis scale is arbitrary but in consistent units.

modes appear in the spectra.[88] As the band-edges consist of contributions only from the inorganic lead iodide frame (Fig. 4a and b), these high-frequency molecular modes remain absent in the carrier recombination across the band gap. The dominant low-frequency peaks in the range of <150 cm^{-1} can be assigned to the bending and stretching modes of the Pb–I frame for all 2D-perovskites (Fig. S11†).[50] The chemically identical inorganic frame for all perovskites results in mostly similar peak positions in the spectra. The higher frequency peaks originate from the complex coupled dynamics of inorganic and spacer cation sublattices as detailed in the ESI (Section S3).† Interestingly, the most important contributions to the electron–phonon interactions (Fig. 6) correspond to the low frequency part of the 2D perovskite phonon spectrum (Fig. S10†), which includes basically only the lowest frequency cation vibrational mode (Fig. S11†). Therefore, the mechanical coupling between the spacer cations and the perovskite layer also strongly rely on the cation librational modes. A similar conclusion was drawn in ref. 38, where the difference of the electron dynamics between $n = 1$ and $n = 3$ multilayered compounds was attributed to the additional contribution coming from the fast motion of the methylammonium cations, within the cage of the $n = 3$ perovskite lattice.

Partially suppressed structural fluctuations and the consequent narrowing of the electronic band gap distribution over time therefore substantially reduce the electron–phonon coupling strengths in the DJ-phase perovskites. Thus, the analysis of the influence spectra strongly suggests that the enhanced stiffness induced by the stronger mechanical coupling in the (3AMP)PbI_4 perovskite slows down the non-radiative carrier recombination processes by weakening the electron–phonon interactions at room temperature.

The NAC between two energy-states form a wavefunction superposition that further invokes the quantum transition between these states. The elastic electron–phonon scattering destroys the quantum coherence facilitating this process, leading to a loss of the superposition and consequently collapsing the wavefunction to only one of the states.[81] Here, a rapid quantum decoherence over time suppresses the transition probability, enhancing the lifetime of a particular quantum state. Considering the electron–phonon recombination at semiconductor band edges, the faster the decoherence between the VBM and CBM, the longer the expected recombination time. The typical timescale of quantum decoherence in solids is tens of femtoseconds (fs), much faster than the inelastic electron–phonon scattering induced processes. As detailed in the ESI (Section S4),† the calculated pure-dephasing time for all the investigated 2D-perovskites is in the range of 4.8–5.7 fs (Table 1). Due to the very similar pure-decoherence times of RP and DJ-phase perovskites, we conclude that the elastic scattering is not a decisive factor that can explain the distinctly different non-radiative carrier recombination rates of these materials (Fig. 5a).

Finally, we emphasize that observed physical processes that dominate non-radiative carrier recombination rates in different 2D iodide perovskites are non-intuitive. For a particular pair of states, Fermi's golden rule depicts that the recombination rate is inversely proportional to their energy band gap and is proportional to the square of the NAC value.[89,90] Thus, marginally smaller average electronic band gap of (3AMP)PbI_4 compared to RP-phase perovskites should result in a slightly shorter recombination time. However, much larger instantaneous NAC values in $(BA)_2PbI_4$ and $(PEA)_2PbI_4$ as shown in Fig. 5b cause faster electron–hole recombination in these perovskites. Thus, it is apparent that the instantaneous spikes of the non-adiabatic couplings dominantly determine the non-radiative recombination rate of 2D lead-halide perovskites.

We also note that the shorter N–H···I distance in the DJ-phase (Fig. 3c) can help to partially suppress the electron–phonon interactions and polaron coupling strengths as demonstrated for 3D-halide perovskites.[91]

Conclusion

In conclusion, we investigate the room temperature charge carrier dynamics in the representative structures of RP and DJ 2D-perovskites by combining time-domain DFT and NAMD simulations. Our calculations identify the dominant roles of finite-temperature structural fluctuations on the photogenerated carrier lifetime in these materials. The single dicationic spacer molecules in the DJ-phase (3AMP)PbI_4 removes the van der Waals gaps present between the two monocationic spacers in the RP-phase halide perovskites. This, in turn, compacts the spacer cation-inorganic layer stacking and partially suppresses the structural dynamics in the Pb–I layers of (3AMP)PbI_4 under ambient conditions. The reduced equatorial Pb–I–Pb angle distortion and thermal fluctuations in (3AMP)PbI_4 lead to narrowly distributed red-shifted band gaps compared to the RP-phase perovskites. Instantaneous charge localization in $(BA)_2PbI_4$ and $(PEA)_2PbI_4$ results in the frequent opening of the non-adiabatic channels through which photogenerated carriers recombine non-radiatively. In contrast, halogen–halogen electronic coupling between the PbI layers partially helps the DJ-phase valence band charge densities to delocalize along the stacking axis, hindering the carrier recombination process. The longer carrier lifetime for (3AMP)PbI_4 suggests its superior performance over the more widely studied RP-phase perovskites for a range of optoelectronic applications.

This work provides a fundamental understanding of the chemical and physical characteristics of the spacer cations to tune the optoelectronic performances of emerging types of hybrid 2D-perovskites. Replacing monocationic spacer cations with dicationic candidates likely not only suppresses the temperature-induced structural fluctuations but also introduces halogen interactions between the inorganic layers. Consequently, weaker electron–phonon interactions and enhanced charge delocalization across the non-bonded perovskite layers substantially improve the charge carrier dynamics. Detailed knowledge of the dynamic structure–optoelectronic property relationships in these low-dimensional halide perovskites suggests several exciting strategies to enhance the electronic functionalities of these materials. For example, the incorporation of short aromatic ring-based spacer molecules or

more electrostatically active functional groups is one of the approaches that can increase the stacking strength between the dication spacer molecules and inorganic layers, being beneficial for charge carrier dynamics.[24]

Methods

The density functional theory (DFT) calculations and *ab initio* molecular dynamics (AIMD) simulations have been performed using the Vienna *Ab Initio* Simulation Package (VASP).[92,93] The projected augmented wave (PAW) method within a plane-wave basis set with a cut-off energy of 500 eV has been adopted for all static DFT calculations.[94] We use the generalized gradient approximation (GGA) with the Perdew–Burke–Ernzerhof functional (PBE) form to approximate the exchange and correlation interactions.[95] We construct the supercell with four formula units of $(BA)_2PbI_4$ and $(PEA)_2PbI_4$, and eight formula units of $(3AMP)PbI_4$ and relax all the interatomic forces to less than 0.01 eV $Å^{-1}$ during internal structural optimization. We further use the DFT-D3 method as described by Grimme[96] and a $6 \times 6 \times 1$ Γ-centered Monkhorst–Pack[97] mesh for all the 2D-perovskites. To calculate more accurate electronic structures, spin–orbit coupling (SOC) was further applied self-consistently as implemented in VASP.

To investigate the charge carrier dynamics, we apply mixed quantum-classical NAMD simulations with the decoherence-induced surface hopping (DISH) technique.[82,98] In this method the electrons and nuclei are considered as quantum mechanical and semiclassical entities, respectively. Some of us and others have previously used this computational approach to compute the excited-state dynamics of inorganic and hybrid perovskites.[36,38,43,84] In AIMD simulations we use a $2 \times 2 \times 1$ Monkhorst–Pack k-point mesh, a time step of 1 fs and a plane-wave energy cutoff of 400 eV. During AIMD calculations we considered PBE-GGA exchange–correlation functions and DFT-D3 corrections. The 0 K DFT optimized structures are considered as the initial structure for AIMD simulations and heated to 300 K using repeated velocity rescaling for 4 ps. Other 4 ps trajectories were generated using the canonical ensemble to ensure the thermal equilibrium of these systems. Following that, we generate 10 ps trajectories in the microcanonical ensemble and used 4 ps of these trajectories for the nonadiabatic coupling simulations. Note that, as we perform AIMD simulations by keeping the cell parameters the same as their experimental values at room temperature, the present trajectories do not include the effects of volume relaxation. However, as we consider the experimental cell parameters under ambient conditions for performing our AIMD simulations, volume relaxation will not affect the main conclusions of the study. We take into account all 4000 geometries along the AIMD trajectories and 1000 stochastic realizations of the DISH process for each geometry to compute the electron–hole recombination as implemented in the PYXAID code.[83,99] We further evaluate the pure-dephasing time as considered in the optical-response theory for evaluating the decoherence time for these materials.[100] Though recent work emphasized the importance of SOC in nonradiative charge recombination, we have excluded this effect in our simulations as such computation significantly increases the computational cost.[101] Another strong approximation is the disregard of the excitonic effects that are present in all 2D halide perovskites. Proper incorporation of these effects requires time-dependent Bethe–Salpeter theory for dynamic lattices, which is an active current area of research. However, due to the fundamental methodological complexities such approaches are not completely developed and numerically feasible yet. We include more details on our computational methods in Section S5 of the ESI file.†

Conflicts of interest

There are no conflicts to declare.

Acknowledgements

The work at the Los Alamos National Laboratory (LANL) was supported by the LANL LDRD program. This work was done in part at the Center for Nonlinear Studies (CNLS) and the Center for Integrated Nanotechnologies (CINT), a U.S. Department of Energy and Office of Basic Energy Sciences user facility, at LANL. This research used resources provided by the LANL Institutional Computing Program. The Los Alamos National Laboratory is operated by Triad National Security, LLC, for the National Nuclear Security Administration of the U.S. Department of Energy (Contract No. 89233218NCA000001). J. E. acknowledges the financial support from the Institut Universitaire de France.

References

1 G. Grancini and M. K. Nazeeruddin, Dimensional tailoring of hybrid perovskites for photovoltaics, *Nat. Rev. Mater.*, 2019, **4**, 4–22.
2 K. Leng, W. Fu, Y. Liu, M. Chhowalla and K. P. Loh, From bulk to molecularly thin hybrid perovskites, *Nat. Rev. Mater.*, 2020, 1–19.
3 J. Shamsi, A. S. Urban, M. Imran, L. De Trizio and L. Manna, Metal halide perovskite nanocrystals: synthesis, post-synthesis modifications, and their optical properties, *Chem. Rev.*, 2019, **119**, 3296–3348.
4 M. Yuan, L. N. Quan, R. Comin, G. Walters, R. Sabatini, O. Voznyy, S. Hoogland, Y. Zhao, E. M. Beauregard and P. Kanjanaboos, Perovskite energy funnels for efficient light-emitting diodes, *Nat. Nanotechnol.*, 2016, **11**, 872.
5 M. D. Smith, B. A. Connor and H. I. Karunadasa, Tuning the luminescence of layered halide perovskites, *Chem. Rev.*, 2019, **119**, 3104–3139.
6 H. Huang, B. Pradhan, J. Hofkens, M. B. Roeffaers and J. A. Steele, Solar-Driven Metal Halide Perovskite Photocatalysis: Design, Stability, and Performance, *ACS Energy Lett.*, 2020, **5**, 1107–1123.
7 X. Zhu, Y. Lin, Y. Sun, M. C. Beard and Y. Yan, Lead-halide perovskites for photocatalytic α-alkylation of aldehydes, *J. Am. Chem. Soc.*, 2019, **141**, 733–738.

8 Y. Dai, C. Poidevin, C. Ochoa-Hernández, A. A. Auer and H. Tüysüz, A Supported Bismuth Halide Perovskite Photocatalyst for Selective Aliphatic and Aromatic C–H Bond Activation, *Angew. Chem., Int. Ed.*, 2020, **59**, 5788–5796.

9 Y. Wang, L. Song, Y. Chen and W. Huang, Emerging New-Generation Photodetectors Based on Low-Dimensional Halide Perovskites, *ACS Photonics*, 2019, **7**, 10–28.

10 L. N. Quan, Y. Zhao, F. P. García de Arquer, R. Sabatini, G. Walters, O. Voznyy, R. Comin, Y. Li, J. Z. Fan and H. Tan, Tailoring the energy landscape in quasi-2D halide perovskites enables efficient green-light emission, *Nano Lett.*, 2017, **17**, 3701–3709.

11 J. Byun, H. Cho, C. Wolf, M. Jang, A. Sadhanala, R. H. Friend, H. Yang and T.-W. Lee, Efficient Visible Quasi-2D Perovskite Light-Emitting Diodes, *Adv. Mater.*, 2016, **28**, 7515–7520.

12 D. Liang, Y. Peng, Y. Fu, M. J. Shearer, J. Zhang, J. Zhai, Y. Zhang, R. J. Hamers, T. L. Andrew and S. Jin, Color-pure violet-light-emitting diodes based on layered lead halide perovskite nanoplates, *ACS Nano*, 2016, **10**, 6897–6904.

13 Y. Liu, J. Cui, K. Du, H. Tian, Z. He, Q. Zhou, Z. Yang, Y. Deng, D. Chen and X. Zuo, Efficient blue light-emitting diodes based on quantum-confined bromide perovskite nanostructures, *Nat. Photonics*, 2019, 1–5.

14 D. H. Cao, C. C. Stoumpos, O. K. Farha, J. T. Hupp and M. G. Kanatzidis, 2D homologous perovskites as light-absorbing materials for solar cell applications, *J. Am. Chem. Soc.*, 2015, **137**, 7843–7850.

15 H. Tsai, W. Nie, J.-C. Blancon, C. C. Stoumpos, R. Asadpour, B. Harutyunyan, A. J. Neukirch, R. Verduzco, J. J. Crochet and S. Tretiak, High-efficiency two-dimensional Ruddlesden–Popper perovskite solar cells, *Nature*, 2016, **536**, 312.

16 J.-C. Blancon, H. Tsai, W. Nie, C. C. Stoumpos, L. Pedesseau, C. Katan, M. Kepenekian, C. M. M. Soe, K. Appavoo and M. Y. Sfeir, Extremely efficient internal exciton dissociation through edge states in layered 2D perovskites, *Science*, 2017, **355**, 1288–1292.

17 Y. Cao, N. Wang, H. Tian, J. Guo, Y. Wei, H. Chen, Y. Miao, W. Zou, K. Pan and Y. He, Perovskite light-emitting diodes based on spontaneously formed submicrometre-scale structures, *Nature*, 2018, **562**, 249–253.

18 J. Feng, C. Gong, H. Gao, W. Wen, Y. Gong, X. Jiang, B. Zhang, Y. Wu, Y. Wu and H. Fu, Single-crystalline layered metal-halide perovskite nanowires for ultrasensitive photodetectors, *Nat. Electron.*, 2018, **1**, 404–410.

19 H. Tsai, F. Liu, S. Shrestha, K. Fernando, S. Tretiak, B. Scott, D. T. Vo, J. Strzalka and W. Nie, A sensitive and robust thin-film x-ray detector using 2D layered perovskite diodes, *Sci. Adv.*, 2020, **6**, eaay0815.

20 L. Mao, W. Ke, L. Pedesseau, Y. Wu, C. Katan, J. Even, M. R. Wasielewski, C. C. Stoumpos and M. G. Kanatzidis, Hybrid Dion–Jacobson 2D lead iodide perovskites, *J. Am. Chem. Soc.*, 2018, **140**, 3775–3783.

21 Y. Li, J. V. Milic, A. Ummadisingu, J.-Y. Seo, J.-H. Im, H.-S. Kim, Y. Liu, M. I. Dar, S. M. Zakeeruddin and P. Wang, Bifunctional Organic Spacers for Formamidinium-Based Hybrid Dion–Jacobson Two-Dimensional Perovskite Solar Cells, *Nano Lett.*, 2018, **19**, 150–157.

22 S. Ahmad, P. Fu, S. Yu, Q. Yang, X. Liu, X. Wang, X. Wang, X. Guo and C. Li, Dion-Jacobson phase 2D layered perovskites for solar cells with ultrahigh stability, *Joule*, 2019, **3**, 794–806.

23 B.-E. Cohen, Y. Li, Q. Meng and L. Etgar, Dion–Jacobson Two-Dimensional Perovskite Solar Cells Based on Benzene Dimethanammonium Cation, *Nano Lett.*, 2019, **19**, 2588–2597.

24 X. Li, W. Ke, B. Traoré, P. Guo, I. Hadar, M. Kepenekian, J. Even, C. Katan, C. C. Stoumpos and R. D. Schaller, Two-Dimensional Dion–Jacobson Hybrid Lead Iodide Perovskites with Aromatic Diammonium Cations, *J. Am. Chem. Soc.*, 2019, **141**, 12880–12890.

25 P. Huang, S. Kazim, M. Wang and S. Ahmad, Toward Phase Stability: Dion–Jacobson Layered Perovskite for Solar Cells, *ACS Energy Lett.*, 2019, **4**, 2960–2974.

26 Y. Shang, Y. Liao, Q. Wei, Z. Wang, B. Xiang, Y. Ke, W. Liu and Z. Ning, Highly stable hybrid perovskite light-emitting diodes based on Dion-Jacobson structure, *Sci. Adv.*, 2019, **5**, eaaw8072.

27 T. Niu, H. Ren, B. Wu, Y. Xia, X. Xie, Y. Yang, X. Gao, Y. Chen and W. Huang, Reduced-dimensional perovskite enabled by organic diamine for efficient photovoltaics, *J. Phys. Chem. Lett.*, 2019, **10**, 2349–2356.

28 L. Dou, A. B. Wong, Y. Yu, M. Lai, N. Kornienko, S. W. Eaton, A. Fu, C. G. Bischak, J. Ma and T. Ding, Atomically thin two-dimensional organic-inorganic hybrid perovskites, *Science*, 2015, **349**, 1518–1521.

29 D. B. Mitzi, Synthesis, crystal structure, and optical and thermal properties of $(C_4H_9NH_3)_2MI_4$ (M = Ge, Sn, Pb), *Chem. Mater.*, 1996, **8**, 791–800.

30 C. C. Stoumpos, D. H. Cao, D. J. Clark, J. Young, J. M. Rondinelli, J. I. Jang, J. T. Hupp and M. G. Kanatzidis, Ruddlesden–Popper hybrid lead iodide perovskite 2D homologous semiconductors, *Chem. Mater.*, 2016, **28**, 2852–2867.

31 C. Katan, N. Mercier and J. Even, Quantum and dielectric confinement effects in lower-dimensional hybrid perovskite semiconductors, *Chem. Rev.*, 2019, **119**, 3140–3192.

32 J.-C. Blancon, A. V. Stier, H. Tsai, W. Nie, C. C. Stoumpos, B. Traore, L. Pedesseau, M. Kepenekian, F. Katsutani and G. Noe, Scaling law for excitons in 2D perovskite quantum wells, *Nat. Commun.*, 2018, **9**, 1–10.

33 J. Leveillee, C. Katan, J. Even, D. Ghosh, W. Nie, A. D. Mohite, S. Tretiak, A. Schleife and A. J. Neukirch, Tuning electronic structure in layered hybrid perovskites with organic spacer substitution, *Nano Lett.*, 2019, **19**, 8732–8740.

34 Y. Chen, Y. Sun, J. Peng, W. Zhang, X. Su, K. Zheng, T. Pullerits and Z. Liang, Tailoring Organic Cation of 2D

Air-Stable Organometal Halide Perovskites for Highly Efficient Planar Solar Cells, *Adv. Energy Mater.*, 2017, **7**, 1700162.

35 X. Gong, O. Voznyy, A. Jain, W. Liu, R. Sabatini, Z. Piontkowski, G. Walters, G. Bappi, S. Nokhrin and O. Bushuyev, Electron–phonon interaction in efficient perovskite blue emitters, *Nat. Mater.*, 2018, **17**, 550.

36 D. Ghosh, A. J. Neukirch and S. Tretiak, Optoelectronic Properties of Two-Dimensional Bromide Perovskites: Influences of Spacer Cations, *J. Phys. Chem. Lett.*, 2020, **11**, 2955–2964.

37 S.-F. Zhang, X.-K. Chen, A.-M. Ren, H. Li and J.-L. Bredas, Impact of Organic Spacers on the Carrier Dynamics in 2D Hybrid Lead-Halide Perovskites, *ACS Energy Lett.*, 2018, **4**, 17–25.

38 Z. Zhang, W.-H. Fang, M. V. Tokina, R. Long and O. V. Prezhdo, Rapid decoherence suppresses charge recombination in multi-layer 2D halide perovskites: time-domain *ab initio* analysis, *Nano Lett.*, 2018, **18**, 2459–2466.

39 K. Abdel-Baki, F. Boitier, H. Diab, G. Lanty, K. Jemli, F. Lédée, D. Garrot, E. Deleporte and J. Lauret, Exciton dynamics and non-linearities in two-dimensional hybrid organic perovskites, *J. Appl. Phys.*, 2016, **119**, 064301.

40 Z. Zhang, W.-H. Fang, R. Long and O. V. Prezhdo, Exciton Dissociation and Suppressed Charge Recombination at 2D Perovskite Edges: Key Roles of Unsaturated Halide Bonds and Thermal Disorder, *J. Am. Chem. Soc.*, 2019, **141**, 15557–15566.

41 D. Ghosh, P. Walsh Atkins, M. S. Islam, A. B. Walker and C. Eames, Good Vibrations: Locking of Octahedral Tilting in Mixed-Cation Iodide Perovskites for Solar Cells, *ACS Energy Lett.*, 2017, **2**, 2424–2429.

42 D. Ghosh, A. R. Smith, A. B. Walker and M. S. Islam, Mixed A-cation perovskites for solar cells: atomic-scale insights into structural distortion, hydrogen bonding, and electronic properties, *Chem. Mater.*, 2018, **30**, 5194–5204.

43 D. Ghosh, D. Acharya, L. Zhou, W. Nie, O. V. Prezhdo, S. Tretiak and A. J. Neukirch, Lattice Expansion in Hybrid Perovskites: Effect on Optoelectronic Properties and Charge Carrier Dynamics, *J. Phys. Chem. Lett.*, 2019, **10**, 5000–5007.

44 F. Thouin, D. A. Valverde-Chávez, C. Quarti, D. Cortecchia, I. Bargigia, D. Beljonne, A. Petrozza, C. Silva and A. R. S. Kandada, Phonon coherences reveal the polaronic character of excitons in two-dimensional lead halide perovskites, *Nat. Mater.*, 2019, **18**, 349–356.

45 T. Schmitt, S. Bourelle, N. Tye, G. Soavi, A. D. Bond, S. Feldmann, B. Traoré, C. Katan, J. Even and S. E. Dutton, Control of Crystal Symmetry Breaking with Halogen-Substituted Benzylammonium in Layered Hybrid Metal-Halide Perovskites, *J. Am. Chem. Soc.*, 2020, **142**, 5060–5067.

46 M.-H. Tremblay, J. Bacsa, B. Zhao, F. Pulvirenti, S. Barlow and S. R. Marder, Structures of $(4\text{-Y-}C_6H_4CH_2NH_3)_2PbI_4$ {Y = H, F, Cl, Br, I}: Tuning of Hybrid Organic Inorganic Perovskite Structures from Ruddlesden–Popper to Dion–Jacobson Limits, *Chem. Mater.*, 2019, **31**, 6145–6153.

47 H. Tsai, C. Liu, E. Kinigstein, M. Li, S. Tretiak, M. Cotlet, X. Ma, X. Zhang and W. Nie, Critical Role of Organic Spacers for Bright 2D Layered Perovskites Light-Emitting Diodes, *Adv. Sci.*, 2020, **7**, 1903202.

48 A. Lemmerer and D. G. Billing, Synthesis, characterization and phase transitions of the inorganic–organic layered perovskite-type hybrids $[(C_nH_{2n+1}NH_3)_2PbI_4]$, n= 7, 8, 9 and 10, *Dalton Trans.*, 2012, **41**, 1146–1157.

49 D. G. Billing and A. Lemmerer, Synthesis, characterization and phase transitions in the inorganic–organic layered perovskite-type hybrids $[(C_nH_{2n+1}NH_3)_2PbI_4]$, n= 4, 5 and 6, *Acta Crystallogr., Sect. B: Struct. Sci.*, 2007, **63**, 735–747.

50 B. Dhanabalan, Y.-C. Leng, G. Biffi, M.-L. Lin, P.-H. Tan, I. Infante, L. Manna, M. P. Arciniegas and R. Krahne, Directional Anisotropy of the Vibrational Modes in 2D-Layered Perovskites, *ACS Nano*, 2020, **14**, 4689–4697.

51 S. Yang, W. Niu, A.-L. Wang, Z. Fan, B. Chen, C. Tan, Q. Lu and H. Zhang, Ultrathin two-dimensional organic–inorganic hybrid perovskite nanosheets with bright, tunable photoluminescence and high stability, *Angew. Chem., Int. Ed.*, 2017, **56**, 4252–4255.

52 Y.-Q. Zhao, Q.-R. Ma, B. Liu, Z.-L. Yu, J. Yang and M.-Q. Cai, Layer-dependent transport and optoelectronic property in two-dimensional perovskite:$(PEA)_2PbI_4$, *Nanoscale*, 2018, **10**, 8677–8688.

53 S. S. Batsanov, Van der Waals radii of elements, *Inorg. Mater.*, 2001, **37**, 871–885.

54 J. Even, L. Pedesseau, J.-M. Jancu and C. Katan, Importance of spin–orbit coupling in hybrid organic/inorganic perovskites for photovoltaic applications, *J. Phys. Chem. Lett.*, 2013, **4**, 2999–3005.

55 S. Meloni, G. Palermo, N. Ashari-Astani, M. Grätzel and U. Rothlisberger, Valence and conduction band tuning in halide perovskites for solar cell applications, *J. Mater. Chem. A*, 2016, **4**, 15997–16002.

56 A. Amat, E. Mosconi, E. Ronca, C. Quarti, P. Umari, M. K. Nazeeruddin, M. Grätzel and F. De Angelis, Cation-induced Band-gap Tuning in Organohalide Perovskites: Interplay of Spin–orbit Coupling and Octahedra Tilting, *Nano Lett.*, 2014, **14**, 3608–3616.

57 J. Even, L. Pedesseau and C. Katan, Comment on "Density functional theory analysis of structural and electronic properties of orthorhombic perovskite $CH_3NH_3PbI_3$" by Y. Wang *et al.*, Phys. Chem. Chem. Phys., 2014, 16, 1424–1429, *Phys. Chem. Chem. Phys.*, 2014, **16**, 8697–8698.

58 J. Even, L. Pedesseau, J.-M. Jancu and C. Katan, DFT and k·p modelling of the phase transitions of lead and tin halide perovskites for photovoltaic cells, *Phys. Status Solidi RRL*, 2014, **8**, 31–35.

59 B. Traore, L. Pedesseau, L. Assam, X. Che, J.-C. Blancon, H. Tsai, W. Nie, C. C. Stoumpos, M. G. Kanatzidis and S. Tretiak, Composite nature of layered hybrid perovskites: assessment on quantum and dielectric confinements and band alignment, *ACS Nano*, 2018, **12**, 3321–3332.

60 J. L. Knutson, J. D. Martin and D. B. Mitzi, Tuning the band gap in hybrid tin iodide perovskite semiconductors using structural templating, *Inorg. Chem.*, 2005, **44**, 4699–4705.
61 L. Pedesseau, D. Sapori, B. Traore, R. Robles, H.-H. Fang, M. A. Loi, H. Tsai, W. Nie, J.-C. Blancon and A. Neukirch, Advances and promises of layered halide hybrid perovskite semiconductors, *ACS Nano*, 2016, **10**, 9776–9786.
62 D. Zhao, H. Hu, R. Haselsberger, R. A. Marcus, M.-E. Michel-Beyerle, Y. M. Lam, J.-X. Zhu, C. La-o vorakiat, M. C. Beard and E. E. Chia, Monitoring Electron–Phonon Interactions in Lead Halide Perovskites Using Time-Resolved THz Spectroscopy, *ACS Nano*, 2019, **13**, 8826–8835.
63 A. D. Wright, C. Verdi, R. L. Milot, G. E. Eperon, M. A. Pérez-Osorio, H. J. Snaith, F. Giustino, M. B. Johnston and L. M. Herz, Electron–phonon coupling in hybrid lead halide perovskites, *Nat. Commun.*, 2016, **7**, 1–9.
64 C. Katan, A. D. Mohite and J. Even, Entropy in halide perovskites, *Nat. Mater.*, 2018, **17**, 377–379.
65 Y. Zhou, L. You, S. Wang, Z. Ku, H. Fan, D. Schmidt, A. Rusydi, L. Chang, L. Wang and P. Ren, Giant photostriction in organic–inorganic lead halide perovskites, *Nat. Commun.*, 2016, **7**, 1–8.
66 C. Quarti, E. Mosconi and F. De Angelis, Structural and Electronic Properties of Organo-halide Hybrid Perovskites from *Ab Initio* Molecular Dynamics, *Phys. Chem. Chem. Phys.*, 2015, **17**, 9394–9409.
67 T. Steiner, The hydrogen bond in the solid state, *Angew. Chem., Int. Ed.*, 2002, **41**, 48–76.
68 Y. Kawashima, K. Sawada, T. Nakajima and M. Tachikawa, A path integral molecular dynamics study on intermolecular hydrogen bond of acetic acid–arsenic acid anion and acetic acid–phosphoric acid anion clusters, *J. Comput. Chem.*, 2019, **40**, 172–180.
69 P. Durlak, C. A. Morrison, D. S. Middlemiss and Z. Latajka, Car-Parrinello and path integral molecular dynamics study of the hydrogen bond in the chloroacetic acid dimer system, *J. Chem. Phys.*, 2007, **127**, 064304.
70 B. Walker and A. Michaelides, Direct assessment of quantum nuclear effects on hydrogen bond strength by constrained-centroid *ab initio* path integral molecular dynamics, *J. Chem. Phys.*, 2010, **133**, 174306.
71 L. Zhou, A. J. Neukirch, D. J. Vogel, D. S. Kilin, L. Pedesseau, M. A. Carignano, A. D. Mohite, J. Even, C. Katan and S. Tretiak, Density of states broadening in $CH_3NH_3PbI_3$ hybrid perovskites understood from *ab initio* molecular dynamics simulations, *ACS Energy Lett.*, 2018, **3**, 787–793.
72 J. Yin, P. Maity, L. Xu, A. M. El-Zohry, H. Li, O. M. Bakr, J.-L. Brédas and O. F. Mohammed, Layer-dependent Rashba band splitting in 2D hybrid perovskites, *Chem. Mater.*, 2018, **30**, 8538–8545.
73 D. Meggiolaro and F. De Angelis, First-Principles Modeling of Defects in Lead Halide Perovskites: Best Practices and Open Issues, *ACS Energy Lett.*, 2018, **3**, 2206–2222.
74 J. He, W.-H. Fang, R. Long and O. V. Prezhdo, Increased Lattice Stiffness Suppresses Nonradiative Charge Recombination in $MAPbI_3$ Doped with Larger Cations: Time-Domain *Ab Initio* Analysis, *ACS Energy Lett.*, 2018, **3**, 2070–2076.
75 D. Lu, G. Lv, Z. Xu, Y. Dong, X. Ji and Y. Liu, Thiophene-based Two-Dimensional Dion–Jacobson Perovskite Solar Cells with over 15% Efficiency, *J. Am. Chem. Soc.*, 2020, **142**, 11114–11122.
76 M. Chen, M.-G. Ju, M. Hu, Z. Dai, Y. Hu, Y. Rong, H. Han, X. C. Zeng, Y. Zhou and N. P. Padture, Lead-Free Dion–Jacobson Tin Halide Perovskites for Photovoltaics, *ACS Energy Lett.*, 2018, **4**, 276–277.
77 J. Jankowska, R. Long and O. V. Prezhdo, Quantum dynamics of photogenerated charge carriers in hybrid perovskites: dopants, grain boundaries, electric order, and other realistic aspects, *ACS Energy Lett.*, 2017, **2**, 1588–1597.
78 A. Nijamudheen and A. V. Akimov, Criticality of symmetry in rational design of chalcogenide perovskites, *J. Phys. Chem. Lett.*, 2017, **9**, 248–257.
79 W. Li, J. Tang, D. Casanova and O. V. Prezhdo, Time-domain *ab initio* analysis rationalizes the unusual temperature dependence of charge carrier relaxation in lead halide perovskite, *ACS Energy Lett.*, 2018, **3**, 2713–2720.
80 C.-J. Tong, L. Li, L.-M. Liu and O. V. Prezhdo, Long Carrier Lifetimes in PbI_2-Rich Perovskites Rationalized by *Ab Initio* Nonadiabatic Molecular Dynamics, *ACS Energy Lett.*, 2018, **3**, 1868–1874.
81 A. J. Neukirch, K. Hyeon-Deuk and O. V. Prezhdo, Time-domain *ab initio* modeling of excitation dynamics in quantum dots, *Coord. Chem. Rev.*, 2014, **263**, 161–181.
82 C. F. Craig, W. R. Duncan and O. V. Prezhdo, Trajectory surface hopping in the time-dependent Kohn-Sham approach for electron-nuclear dynamics, *Phys. Rev. Lett.*, 2005, **95**, 163001.
83 A. V. Akimov and O. V. Prezhdo, The PYXAID program for non-adiabatic molecular dynamics in condensed matter systems, *J. Chem. Theory Comput.*, 2013, **9**, 4959–4972.
84 R. Long, J. Liu and O. V. Prezhdo, Unravelling the effects of grain boundary and chemical doping on electron–hole recombination in $CH_3NH_3PbI_3$ perovskite by time-domain atomistic simulation, *J. Am. Chem. Soc.*, 2016, **138**, 3884–3890.
85 J. He, A. S. Vasenko, R. Long and O. V. Prezhdo, Halide composition controls electron–hole recombination in cesium–lead halide perovskite quantum dots: a time domain *ab initio* study, *J. Phys. Chem. Lett.*, 2018, **9**, 1872–1879.
86 W. Li, Y.-Y. Sun, L. Li, Z. Zhou, J. Tang and O. V. Prezhdo, Control of charge recombination in perovskites by oxidation state of halide vacancy, *J. Am. Chem. Soc.*, 2018, **140**, 15753–15763.
87 W. Li, J. Liu, F.-Q. Bai, H.-X. Zhang and O. V. Prezhdo, Hole trapping by iodine interstitial defects decreases free carrier losses in perovskite solar cells: a time-domain *ab initio* study, *ACS Energy Lett.*, 2017, **2**, 1270–1278.
88 A. M. Leguy, A. R. Goñi, J. M. Frost, J. Skelton, F. Brivio, X. Rodríguez-Martínez, O. J. Weber, A. Pallipurath, M. I. Alonso and M. Campoy-Quiles, Dynamic disorder, phonon lifetimes, and the assignment of modes to the

vibrational spectra of methylammonium lead halide perovskites, *Phys. Chem. Chem. Phys.*, 2016, **18**, 27051–27066.

89 R. Englman and J. Jortner, The energy gap law for non-radiative decay in large molecules, *J. Lumin.*, 1970, **1**, 134–142.

90 R. Long, O. V. Prezhdo and W. Fang, Nonadiabatic charge dynamics in novel solar cell materials, *Wiley Interdiscip. Rev.: Comput. Mol. Sci.*, 2017, **7**, e1305.

91 C. W. Myung, J. Yun, G. Lee and K. S. Kim, A New Perspective on the Role of A-Site Cations in Perovskite Solar Cells, *Adv. Energy Mater.*, 2018, **8**, 1702898.

92 G. Kresse and J. Hafner, Ab initio molecular dynamics for liquid metals, *Phys. Rev. B: Condens. Matter Mater. Phys.*, 1993, **47**, 558.

93 G. Kresse and J. Hafner, Ab initio molecular-dynamics simulation of the liquid-metal–amorphous-semiconductor transition in germanium, *Phys. Rev. B: Condens. Matter Mater. Phys.*, 1994, **49**, 14251.

94 G. Kresse and D. Joubert, From ultrasoft pseudopotentials to the projector augmented-wave method, *Phys. Rev. B: Condens. Matter Mater. Phys.*, 1999, **59**, 1758.

95 J. P. Perdew, K. Burke and M. Ernzerhof, Generalized Gradient Approximation Made Simple, *Phys. Rev. Lett.*, 1996, **77**, 3865.

96 S. Grimme, J. Antony, S. Ehrlich and H. Krieg, A consistent and accurate *ab initio* parametrization of density functional dispersion correction (DFT-D) for the 94 elements H-Pu, *J. Chem. Phys.*, 2010, **132**, 154104.

97 H. J. Monkhorst and J. D. Pack, Special points for Brillouin-zone integrations, *Phys. Rev. B: Solid State*, 1976, **13**, 5188.

98 H. M. Jaeger, S. Fischer and O. V. Prezhdo, Decoherence-induced surface hopping, *J. Chem. Phys.*, 2012, **137**, 22A545.

99 A. V. Akimov and O. V. Prezhdo, Advanced capabilities of the PYXAID program: integration schemes, decoherence effects, multiexcitonic states, and field-matter interaction, *J. Chem. Theory Comput.*, 2014, **10**, 789–804.

100 P. Hamm, *Principles of Nonlinear Optical Spectroscopy: A Practical Approach*, University of Zurich, 2005, 41, p. 77.

101 W. Li, L. Zhou, O. V. Prezhdo and A. V. Akimov, Spin–orbit interactions greatly accelerate nonradiative dynamics in lead halide perovskites, *ACS Energy Lett.*, 2018, **3**, 2159–2166.

